

11<sup>th</sup> ANKARA INTERNATIONAL AEROSPACE CONFERENCE  
8-10 September 2021 - METU, Ankara TURKEY

**AIAC-2021-082**

## **Investigation of RAE-M2129 S-Shaped Intake with Computational Fluid Dynamics**

Mehmet Erdemli<sup>1</sup>  
METU  
Ankara, Turkey

Çağrı Alim Seyit Metin<sup>2</sup>  
TAI  
Ankara, Turkey

İsmail Ozan Sert<sup>3</sup>  
TOBB ETU  
Ankara, Turkey

Onur Baş<sup>4</sup>  
TEDU  
Ankara, Turkey

### **ABSTRACT**

This study investigates the high-curvature S-shaped RAE M2129 intake in subsonic and transonic regimes using Reynolds-Averaged Navier-Stokes equation. Two cases are investigated to simulate high mass flow and low mass flow engine demand. The main purpose is in focus that comprehensive validation of RAE M2129 intake with global and local flow properties. It is found that pressure recovery and pressure distribution along the wall are well captured for all solvers, i.e. CFD++, StarCCM+ and HISA-OpenFOAM. The location of shock and flow separation is consistently similar for the solvers and the experiment. However, the distortion coefficient is found slightly departed from the experimental results. Furthermore, the variation of total pressure on the engine face is again found slightly different for each solver which can also be related with the difference of distortion parameter. These findings may be a guide for a validation methodology and procedures of subsonic/transonic intake with high-curvature S-duct to improve necessary skills.

### **INTRODUCTION**

Engine intake is an essential part of the aircraft that directly interface both with the internal and external airflow. The intake should provide air to the engine with desired quantity and quality (Miller & Addington, 2004; Hamstra et al., 2000; Mattingly, 2006). The primary purpose of an intake is to sustain air to engine from freestream with minimum total pressure loss at a given Mach number range. Nevertheless, engine performance is also affected from non-uniformity of flow, which can be measured with parameters such as distortion and swirl. The distortion of the flow is one of the challenging subject for an intake (Anderson & Gibb, 1993; Bowditch & Coltrin, 1983). The boundary layer separation or highly distorted flow could cause severe problems and engine surge (Küçük, 2015). Hence, all of these parameters should be estimated for the possible flight envelope in the design phase to guarantee the engine health and performance.

Numerical methods have become essential components of the design phases of an intake in last decades by developing computational technology. Computational Fluid Dynamics (CFD) allows us to determine the global parameters as well as local flow properties. Unlike the experimental studies, CFD has capability to present the flow information in detail for the whole computational domain. However, CFD analyses for engine intakes can be challenging due to

---

<sup>1</sup> MSc. Student in Mechanical Engineering, Email: mehmet.erdemli@metu.edu.tr

<sup>2</sup> Computational Aerodynamics Engineer in Turkish Aerospace Industry, Email: cagrialimseyit.metin@tai.com.tr

<sup>3</sup> PhD. Student in Aerospace Engineering, Email: isert@tai.com.tr

<sup>4</sup> Assistant Prof. in Aerospace Engineering, Email: onur.bas@tedu.edu.tr

complicated flow characteristic. Solver properties and implementations have an impact on convergence speed and accuracy.

A well-known intake benchmark case, namely the Royal Aircraft Establishment intake model 2129 (RAE M2129), is studied numerically in this study (AGARD, 1991). The flow in the RAE M2129 intake is complex and challenging for CFD solvers. Accelerated flow near the lip of the cowl reaches supersonic flow and is terminated by a  $\lambda$ -shock (Menzies, 2002a; Menzies, 2002b). Afterwards, deceleration of the flow causes boundary layer separation by an adverse pressure gradient vicinity of first bend of the S-duct due to high curvature of the intake (Lee et al., 2019; Menzies, 2002a; Menzies, 2002b). The pair of counter-rotating vortices on the compressor face are found to be the main source of total pressure loss of the intake (Tanguy et al., 2017; Wellborn et al., 1994; Reichert & Wendt, 1996; Garnier et al., 2012). The capturing separation location and secondary flow are important subjects for CFD solvers.

The purpose of this study is to conduct a comprehensive validation with pressure recovery, distortion coefficient, and pressure distribution along the intake walls. With this motivation, we conducted Reynolds-Averaged Navier-Stokes simulation on different solvers, such as CFD++, StarCCM+, and HISA-OpenFOAM for two different cases. These two cases are characterized by low mass flow rate and high mass flow rate at engine face. We also focus on capturing the local flow properties such as boundary layer separation and local shocks.

## COMPUTATIONAL METHOD

### Geometry of RAE M2129 Intake

Geometry of RAE M2129 intake can be divided into three main parts. These are cowl, diffuser (s-duct) and engine aerodynamic interface plane (AIP). The intake has circular cross sections from beginning to end, and the cross sections are constant for a diameter upstream of throat and a diameter downstream of diffuser. Constant cross sections are connected with serpentine diffuser as shown in Figure 1. Cowl of the intake is an ellipse with  $\frac{1}{4}$  ratio. Curve of centerline for serpentine diffuser and distribution of radius can be obtained with following equations (AGARD,1991);

$$Z_{cl} = -\Delta Z \left[ 1 - \cos \frac{\pi X_{cl}}{L} \right] \frac{R - R_i}{R_{ef} - R_i} = 3 \left( 1 - \frac{X_{cl}}{L} \right)^4 - 4 \left( 1 - \frac{X_{cl}}{L} \right)^3 + 1$$

with parameters as given below;

$$R_1(\text{Throat Radius}) \rightarrow 0.0644 \text{ m}$$

$$\frac{R_{ef}}{R_1} \rightarrow 1.183 \quad \frac{L}{R_1} \rightarrow 7.1 \quad \frac{\Delta Z}{R_1} \rightarrow 2.13$$

### Computational Domain and Boundary Conditions

Three-dimensional Reynolds-Averaged Navier-Stokes equation set is solved in order to investigate subsonic/transonic RAE M2129 intake. The computational domain on the outlet of the intake is extended beyond the engine compressor face (or aerodynamic interface plane) to reduce interference of the outlet boundary condition. The freestream boundary is extended to  $15D_{\max}$ , which  $D_{\max} = 0.1524 \text{ m}$  is the reference length of the intake. The freestream size is chosen large enough to allow propagation of waves from reflected object inside the domain (Figure 1).

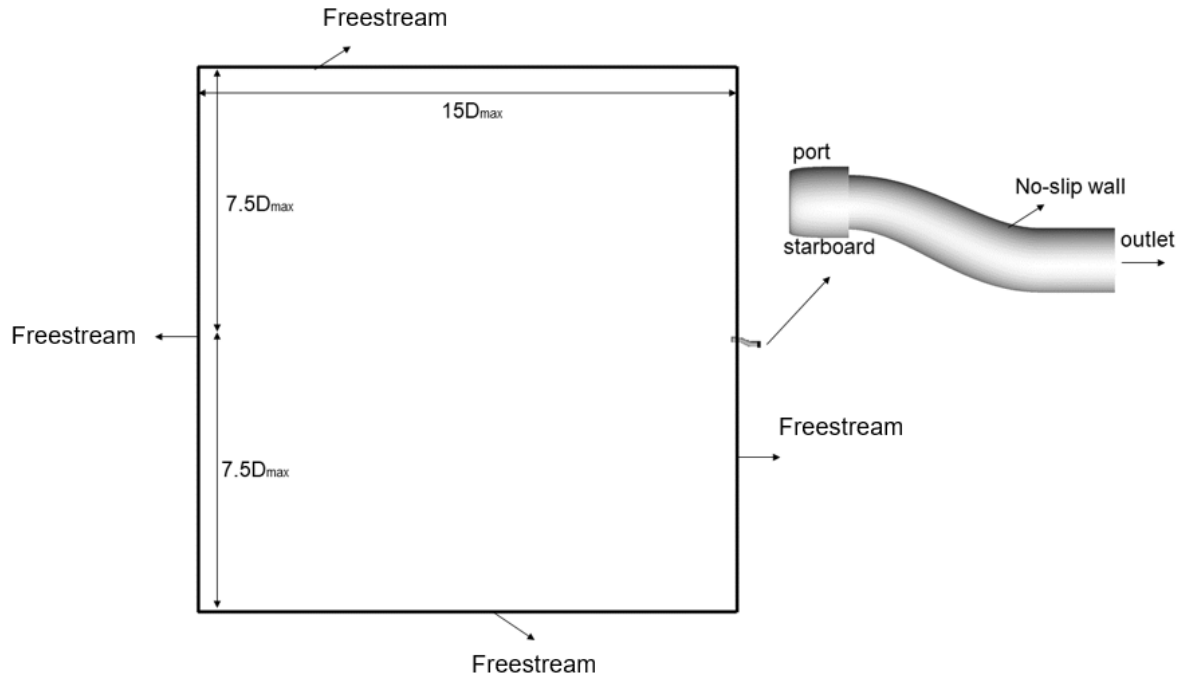


**Figure 1:** Computational domain and boundary conditions, and geometry of RAE M2129

The intake and hub of the compressor are modelled as adiabatic no-slip wall condition. These walls are reflected type of boundary conditions in a transonic or supersonic regime. On the other hand, the freestream boundary is assigned a non-reflecting characteristic farfield boundary condition. This type of boundary condition allows us to reduce the farfield size (i.e.,  $\approx 15D_{\max}$ ) with transfer waves without reflecting inside the domain. The engine outlet boundary condition is assumed to be subsonic with constant static pressure condition. It is also assumed that the swirl effect propagating upstream due to the compressor fan can be neglected on the boundary face, therefore the static pressure condition only corresponds to engine demand. The engine outlet boundary is located far enough from the aerodynamic interface plane (i.e., compressor face) to make these assumptions valid (Menzies et al., 2002a). In addition, to capture the engine mass flow rate more accurately, target mass flow rates are specified on CFD++ and StarCCM+. The magnitude of static pressure is adjusted automatically in these solvers to match the desired mass flow rate.

	High Mass Flow Rate	Low Mass Flow Rate
$M_{\infty}$	0.21	0.21
$P_{\infty}$	98152.29 Pa	98073.45 Pa
$T_{\infty}$	290.438 K	290.438 K
$\dot{m}_{engine\ face}$	2.898 kg/s	2.003 kg/s

**Table 1:** Boundary conditions

Two test cases are investigated in this study as shown in Table 1. First test case is called high mass flow rate (HMFR), whereas the second test case simulates low mass flow rate (LMFR). The mass flow rate can be thought as an engine demand (Menzies et al., 2002a). For both cases, the freestream Mach number, angle of attack  $\alpha = 0^{\circ}$  and sideslip  $\beta = 0^{\circ}$  are the same. The flow is assumed to be calorically perfect, and the total temperature,  $T_{t,\infty} = 293\text{ K}$ , is the same for both cases. The different engine demand is simulated with different freestream static pressure and static pressure on the engine face ratio.

## Spatial and Temporal Resolution

Two different three-dimensional unstructured finite volume meshes are generated to discretize the computational domain. These meshes are named as hybrid and polyhedral according to their cell types. The resolution of the cells are adequately refined to capture desired flow properties. The boundary layer of the intake has 36 layers, where  $y^+ \approx 1$ . Therefore, the wall-treatment of the turbulence model is chosen as no wall-model and whole regions of boundary layer is resolved during the simulation. In addition, the basic quality of the meshes (such as aspect ratio and skewness) are satisfactory good enough for the smooth convergence of the simulation (Table 2).

Mesh-cell type	Hybrid	Polyhedral
Number of cells	$2.8 \times 10^6$	$4.04 \times 10^6$
Maximum aspect ratio	1205	189
Maximum skewness equiangle	0.414	-
Maximum skewness angle	-	$80.7^\circ$
$y^+ _{wall}$	$\approx 1$	$\approx 1$
Number of prism layer	36	36

**Table 2:** Parameters of finite volume meshes

The time discretization of the simulation is steady-state for all analysis. To accelerate the convergence, the local time stepping is applied for each mesh. The maximum pseudo Courant number depends on the specific case but we restrict it to be less than 50 in this study.

## Governing Equations and Solution Methods

The governing equations are discretized with flux-differencing HLLC scheme for inviscid fluxes for HISA and CFD++, Roe FDS scheme for StarCCM+. Second order gradient-limited central differencing for diffusion terms, and steady-state Euler local time stepping for time discretization. All solvers have capability of density based coupled solution. The coupled matrix system is solved GMRES with LUSGS preconditioning for HISA, Gauss-Seidel AMG for CFD++ and StarCCM+ with Weiss&Smith and BCGSM preconditioners respectively. Turbulence properties are modelled with k- $\omega$  SST turbulence model without wall function. The numerical studies are performed in AMD EPYC 7352 48 processors at Turkish Aerospace High Performance Computing Infrastructure.

	HISA	CFD++	StarCCM+
(Pseudo) Max CFL #	25	100	50
Inviscid Flux	HLLC	HLLC	Roe FDS
Gradient (limiter)	LeastSquares (Minmod)	LeastSquares (Minmod)	Venkatakrishnan
Reconstruction	Van Leer	-	-
Jacobian matrices	Matrix-free	Approx. Jacobian	Approx. Jacobian
Preconditioner	LUSGS	Weiss&Smith	BCGSM
Matrix Solution	GMRES	Gauss Seidel AMG	Gauss Seidel AMG
Turbulence model (Wall-model)	k- $\omega$ SST (no wall function)	k- $\omega$ SST (no wall function)	k- $\omega$ SST (no wall function)

**Table 3:** Solution parameters

## Validation and Verification

The experimental study of the RAE M2129 Subsonic/Transonic circular intake is chosen for the validation and verification of the numerical approach (AGARD, 1991). Figure 2 shows pressure distribution along the intake on the starboard side. The local flow properties for the

low mass flow rate is captured successfully up to  $x/D \approx 1$ . The numerical results depart from the experimental result after this point due to three dimensional unsteady effect of flow separation and secondary flow. However, the results obtained with Mesh 3 and Mesh 4 are consistent with each other and that shows the local flow properties are not changing with increasing number of cells.

Similarly, the overall physical behavior along the intake can be captured for the high mass flow demand of the engine. The pressure distribution along the intake did not change when the number of mesh increases from Mesh 3 to Mesh 4. Hence, subsequent section and investigation are reported with mesh called Mesh 3.

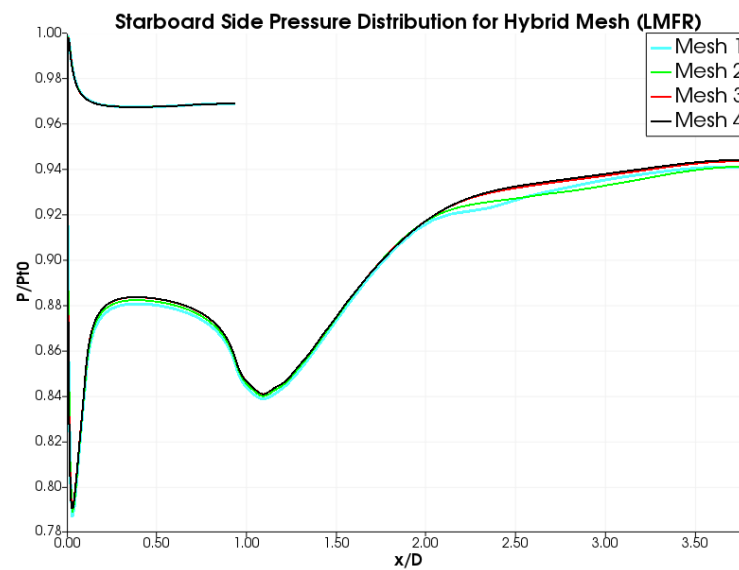


**Fig 2:** The mesh independence and comparison with the experimental result on the starboard side

Mesh dependency study is also conducted for polyhedral mesh structure in order to obtain mesh independent solutions. 5 different poly meshes are generated with different cell numbers as given in Table 4.

	Surface Mesh #	Volume Mesh #
<b>Mesh 1</b>	0.21 E5	0.32 E6
<b>Mesh 2</b>	0.42 E5	0.97 E6
<b>Mesh 3</b>	0.62 E5	1.73 E6
<b>Mesh 4</b>	1.16 E5	4.05 E6
<b>Mesh 5</b>	1.88 E5	8.04 E6

**Table 4:** Number of polyhedral meshes

Low mass flow rate boundary conditions are used for the mesh dependency study. Pressure recovery values at the AIP with different meshes can be seen in Figure 3. The pressure recovery is calculated with mass flow averaged total pressure at the AIP.

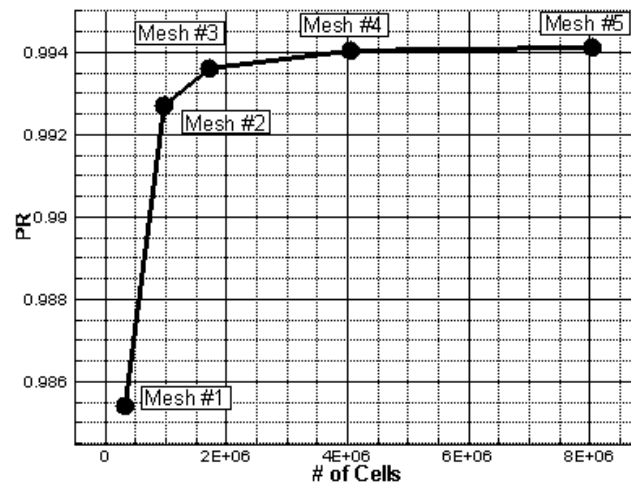


**Fig 3:** Change of PR with different meshes

Mesh dependency study for polyhedral mesh is concluded with comparison of pressure distributions along the starboard side of the duct. Results are presented in Figure 4.

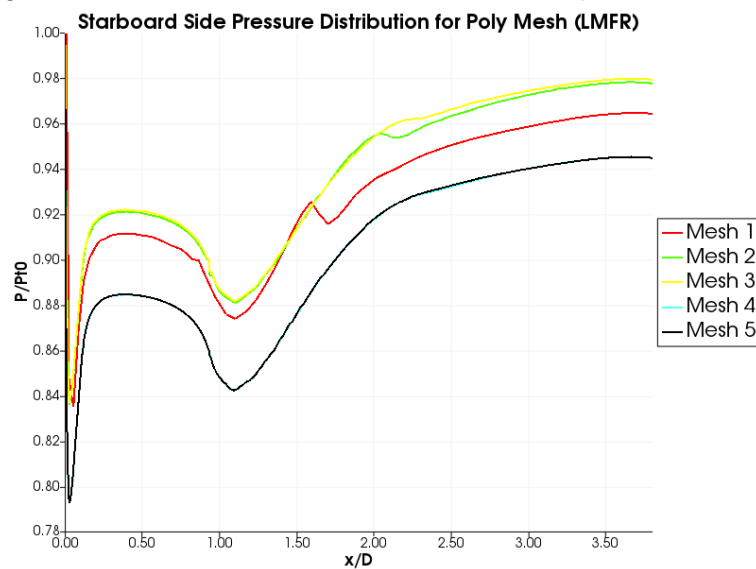


**Fig 4:** Pressure distributions along the starboard side

Finally, it is observed that solution does not change with number of elements after Mesh 4. Hence, Mesh 4 is considered as final mesh structure and shown in Figure 5.

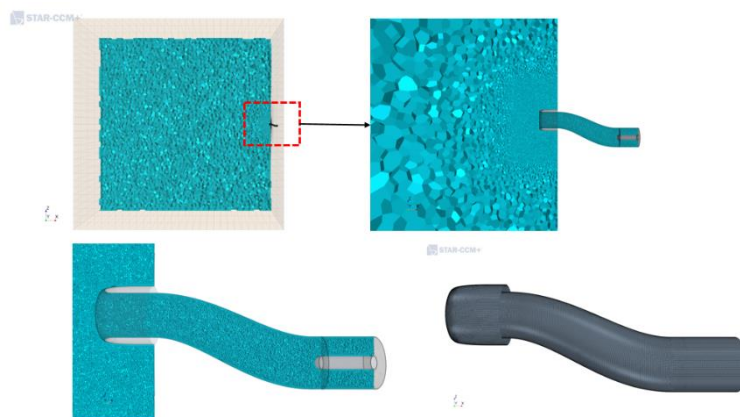


**Fig 5:** Final polyhedral mesh structure

## RESULTS AND DISCUSSION

We investigate the RAE M2129 Subsonic/Transonic circular intake in order to evaluate capabilities and performances of different numerical solvers. The performance of the solver is investigated by the accuracy of the solution, which is determined in terms of global intake parameters (i.e., pressure recovery and desired mass flow rate), distortion parameter on the compressor face and local flow properties. We focus on the two different cases that are low mass flow rate and high mass flow rate. The low mass flow rate corresponds to subsonic flow through the intake and secondary flow is observed on this case (Menzies et al., 2002b). On the other hand, the high mass flow rate corresponds to the flow that reaches locally supersonic (Menzies et al., 2002b). Solutions are obtained with polyhedral mesh for StarCCM+ and hybrid mesh for the other solvers.

### Global Intake Parameters

Mass flow rate and pressure recovery are employed to assess of accuracy of the solvers. Pressure recovery indicates the efficiency of an intake and relates to the loss of useful power. The pressure recovery can be defined as,

$$PR = \frac{\bar{P}_{tAIP}}{\bar{P}_{t\infty}}$$

where  $\bar{P}_{tAIP}$  is the mean total pressure on the Aerodynamic Interface Plane (AIP) , which is an imaginary plane before compressor face, and  $\bar{P}_{t\infty}$  is the mean freestream total pressure. As shown in Table 5, desired mass flow rate and pressure recovery are successfully captured compared to the experimental value where the error is less than 1% in HISA solution for both the high mass flow and the low mass flow demand of the engine. On the other hand, CFD++ and StarCCM+ have capability of target mass flow rate that adjusts the pressure on the engine outlet boundary condition. This type of outlet boundary condition helps to capture the desired mass flow rate accurately. The pressure recoveries of all solvers, on the other hand, can capture the experimental value where the error is less than 2% in the case of the low mass flow rate and the high mass flow rate except CFD++. The pressure recovery of CFD++ over predicts the experimental value in the case of the high mass flow rate.

	High Mass Flow Rate		Low Mass Flow Rate	
	$\dot{m}_{engine}$ (kg/s)	$P_{t,AIP}/P_{t,\infty}$	$\dot{m}_{engine}$ (kg/s)	$P_{t,AIP}/P_{out}$
Experiment (ARA)	2.989	0.92798	2.003	0.98974
HISA	2.976	0.93665	1.992	0.98896
CFD++	2.970	0.95362	2.009	0.99186
StarCCM	2.989	0.94719	2.000	0.99230

**Table 5:** Mass flow rate and pressure recovery

### Distortion on Compressor Face

The loss of the useful power was investigated in previous section. However, the flow on the compressor face also requires uniform flow as much as possible. Performance of an engine rotor blades depend upon upcoming flow uniformity. In this section, we investigate steady-state total distortion coefficient to assess the spatial non-uniformity on the compressor face. The distortion coefficient is defined as,

$$DC(\theta) = \frac{\bar{P}_{t_{AIP}} - \bar{P}_{t_\theta}}{\bar{q}_{t_{AIP}}}$$

where,  $\bar{P}_{t_{AIP}}$  is average total pressure of every points,  $\bar{P}_{t_\theta}$  is average total pressure of points on  $\theta$  angle section, and  $\bar{q}_{t_{AIP}}$  is average dynamic pressure of every points.

	High Mass Flow Rate	Low Mass Flow Rate
	DC(60)	DC(60)
Experiment [ARA]	0.3978	0.226
HISA	0.4258	0.153
CFD++	0.4761	0.1563
StarCCM+	0.5038	0.1409

**Table 6:** Distortion coefficient at  $\theta = 60^\circ$  sector

As shown in Table 6, the distortion coefficients  $DC(60^\circ)$  of all solvers under predict the experimental value for the low mass flow rate. However, StarCCM+ results are smaller than HISA and CFD++. In the case of the high mass flow rate, the solvers found the distortion coefficient  $DC(60^\circ)$  higher than the experimental value. This discrepancy between experimental and numerical distortion coefficients can be related to turbulence modelling and conditions, or steady-state assumption of numerical study. Berens et al. (2012) suggested that the time-dependent solution leads to more accurate results for the distortion coefficient. In order to understand the difference of distortion coefficient between solvers further, we investigate the total pressure distribution on the engine face in Figure 6.

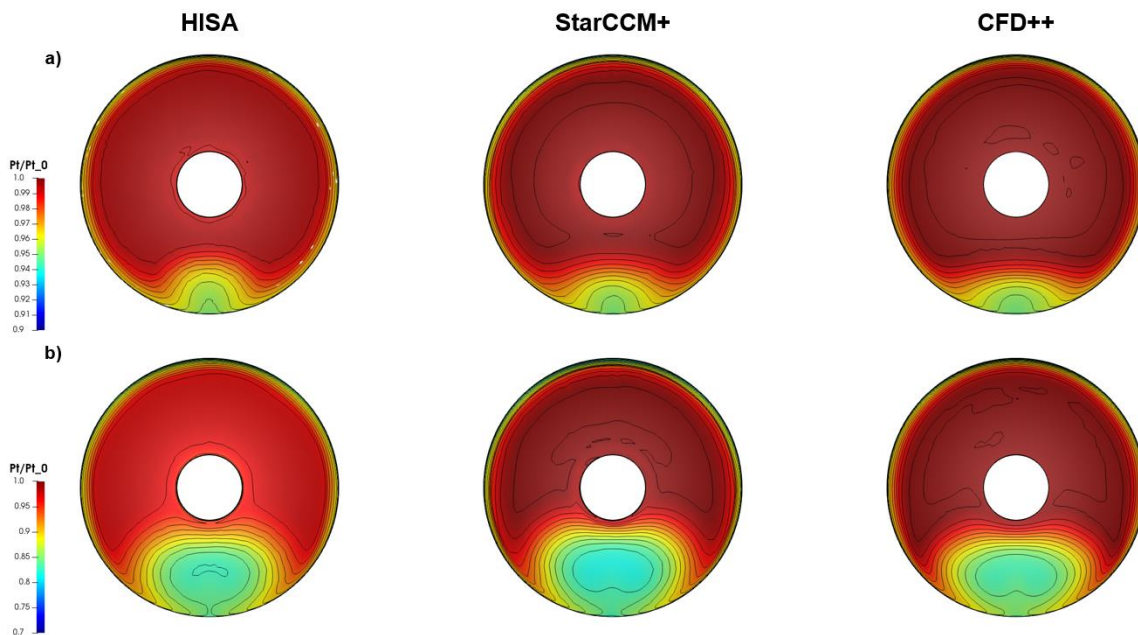


**Fig 6:** Total pressure at the compressor face non-dimensionalized by farfield total pressure and comparison to the experimental study a) LMFR, b) HMFR

The total pressure non-dimensionalized by farfield total pressure is presented in Figure 6 for the low mass flow and the high mass flow demand of the engine. For the low mass flow rate, due to the flow separation and high bending of the duct, counter rotating vortices and related low total-pressure region are observed on starboard side of the duct, which accommodate the worst total pressure sector of  $\theta = 60^\circ$ . The flow separation and corresponding counter rotating vortices could be under-predicted for the low mass flow rate case. As shown in Figure 6, the solution of StarCCM+ shows the smallest change of the total pressure that could be related to under prediction of the  $DC(60^\circ)$  for the StarCCM+ result in



Table 6. Similarly, the changes of the total pressure distribution on the engine face are found similar for HISA and CFD++ solution (Figure 6a). This leads to similar  $DC(60^\circ)$  values of HISA and CFD++ for the low mass flow demand of the engine (Table 5).

In the high mass flow rate, a small separation region is expected in the cowl due the shock boundary layer interaction. In addition, the flow reaches supersonic speeds before the first bend of the intake. Therefore, these losses lead to smaller pressure recovery and higher distortion. The  $DC(60^\circ)$  value of HISA is quite similar to experimental value and the resulting flow behavior on the engine face is successfully captured in HISA solution. On the other hand,  $DC(60^\circ)$  from StarCCM+ and CFD++ over predict the experimental value in the high mass flow demand of the engine.

## Local Flow Properties

The local total pressure distribution through the intake is presented on the starboard side of the intake for the low mass flow and high mass flow engine demand, respectively (Figure 6a and 6b). As mentioned earlier, the low mass flow rate has subsonic flow through the intake, whereas the high mass flow rate has locally supersonic flow in the intake. Following section aims to present these local flow properties in terms of the pressure distribution through the intake.

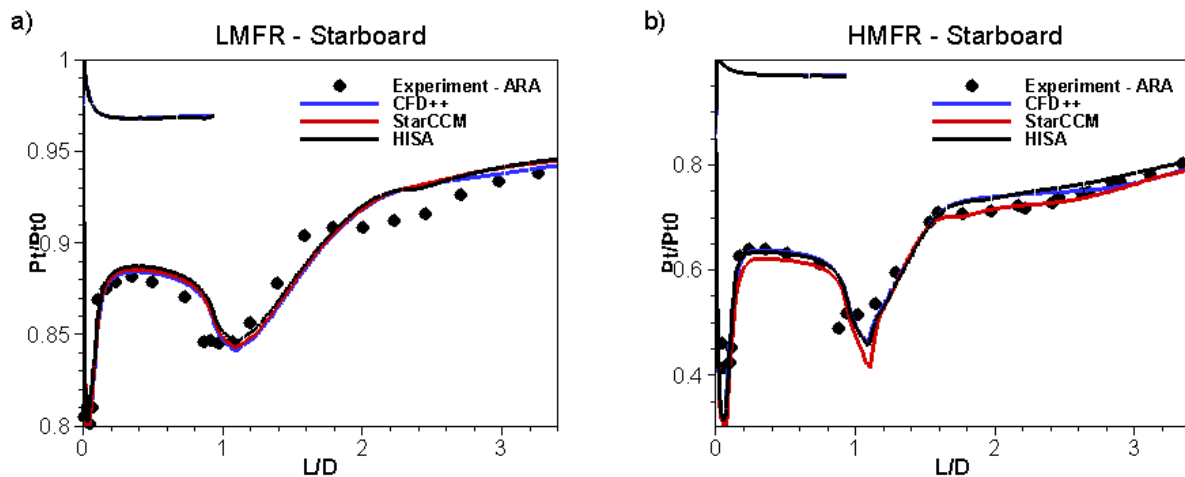


Fig 7: Pressure distribution along the intake a) LMFR, and b) HMFR

For the low mass flow rate, significant energy loss is observed near the leading edge of the intake lip close to  $L/D \approx 0.06$ . The total pressure reaches second lowest value about  $x/D \approx 1$  (Figure 7a). This location accommodates the high curvature of the duct. Due to the generated strong adverse pressure gradient, the separation of the boundary layer and resulting secondary flow are occurred on the starboard side of the intake. The pressure distribution along the intake shows same trend for all solvers. It is also argued that the flow separation and secondary flow remains challenging phenomenon for solvers.

For the high mass flow rate, the pressure reaches the minimum threshold value near the leading edge of the intake lip, which is about  $L/D \approx 0.06$ . (The static pressure to freestream total pressure ratio is smaller than the threshold value,  $P/P_{to} = 0.52$ ). A  $\lambda$ -shock wave occurs near the leading edge of the intake lip because of the acceleration of boundary layer; the boundary layer separate locally due to shock boundary layer interaction. The flow in the starboard side shows another pressure drop about  $x/D \approx 1$  (Figure 4b). The boundary layer on the starboard side accelerates to respond the centrifugal force inside the bend about  $x/D_{max} \approx 1$ . HISA and CFD++ can capture the  $\lambda$ -shock wave near lip and dip of the pressure more

successfully. The numerical results of StarCCM+, HISA and CFD++ can also predict successfully the local supersonic region on the starboard side  $x/D_{\max} \approx 1$ . Afterwards, the high deceleration of boundary layer on the starboard side presents separated flow after the first bend. StarCCM+ shows smaller total pressure loss near  $x/D_{\max} \approx 1$ . The flow becomes three-dimensional and the separation bubble extend through aerodynamic interface. Then, the flow is re-attached afterwards, and secondary flow is generated. The small dip of the pressure distribution  $x/D_{\max} \approx 2$  is a footprint of this behavior and can only be captured by StarCCM+.

## Runtime Comparison

Averaged elapsed time per iteration and total iteration numbers for convergence is compared between the solvers as presented in Table 7. Analysis are completed on the same AMD EPYC 7352 model 2x24-Core processor with 48 cores in total.

	High Mass Flow Rate		Low Mass Flow Rate	
	Total Iteration	Seconds per Iteration	Total Iteration	Seconds per Iteration
HISA	2000	7.5	3000	4.4
CFD++	2500	5.2	1000	5.2
StarCCM+	4000	1.6	2000	1.6

**Table 7:** Runtime comparison of the solvers

StarCCM+ performed faster seconds per iteration than the other solvers approximately 60-80%. On the other hand, HISA is converged in less iterations than CFD++ and StarCCM+ for the high mass flow rate. The low mass flow rate case is converged faster than the high mass flow rate case for CFD++ and StarCCM+ unlike HISA. All in all, StarCCM+ has ~50% faster total elapsed time for the both cases compared with CFD++ and HISA.

## CONCLUSIONS

We investigate the high-curvature S-shaped RAE M2129 intake in subsonic and transonic regimes with CFD++, StarCCM+ and HISA solvers. The capability of these solvers are compared with each other and with the experimental results. We also focus on comprehensive validation of RAE M2129 intake with global and local flow properties. With this motivation, two different cases that are low mass flow rate and high mass flow rate are investigated. For the low mass flow rate, the significant pressure drop near the leading edge can be captured successfully with all solvers. On the other hand, the flow separation and secondary flow are challenging for numerical methods. For the high mass flow rate, the small separation region in the cowl due the  $\lambda$ -shock wave boundary layer interaction can be observed in all solutions. Moreover, the flow reaches the sonic speeds again near the second bend of the duct before the separation occurs. On the other hand, StarCCM+, CFD++ and HISA can predict Pressure Recovery and Distortion Coefficient satisfactory enough. Overall, all solvers can capture the main physics of the intake and have satisfactory agreement with experimental results. Furthermore, we also aim to investigate time-depending capability of these solvers. In order to investigate time-depending oscillatory physical behavior and those capabilities of each solvers, higher resolution methods such as Detached Eddy Simulation (DES) or Wall-Modelled Large Eddy Simulation (WMLES) are planned in the future.

## References

- Anderson, B. H., & Gibb, J., "Study on Vortex Generator Flow Control for the Management of Inlet Distortion," Journal of Propulsion and Power, Vol. 9, No. 3, June 1993
- Berens T. M., Anne-Laure Delot, Chevalier M., Muijden J. V., Waaijer R. A. & Tattersall P., Garteur AD/AG-43 Application of CFD to High Offset Intake Diffusers. Final Report, 2012

- Bowditch, D. N., & Coltrin, R. E., "A Survey of Inlet/Engine Distortion Compatability," AIAA Paper 83-1166, June 1983
- Garnier, E., Leplat, M., Monnier, J. C., and Delva, J., "Flow Control by Pulsed Jet in a Highly Bended S-Duct," 6th AIAA Flow Control Conference, AIAA Paper 2012-3250, 2012.
- Lee, J., Lee S., & Cho J. (2019) *Effect of Inlet Boundary Layer Suction on Flow Distortion in Subsonic Diffusing S-Duct*, International Journal of Aeronautical and Space Sciences, Springer,
- Miller, D., and Addington, G., "Invited: Aerodynamic Flowfield Control Technologies for Highly Integrated Airframe Propulsion Flowpaths," AIAA Paper 2004-2625, June 2004.
- Hamstra, J. W., Miller, D. N., Traux, P. P., Anderson, B. H., and Wend, B. J., "Active Inlet Flow Control Technology Demonstration," ICAS Paper 2000-6.11.2, Aug.–Sept. 2000
- Mattingly, J.D. (2006) *Elements of propulsion: gas turbines and rockets* , AIAA Education Series, 3<sup>rd</sup> Ed., 2006
- Menzies R.D.D. (2002a) *Investigation of S-shaped intake aerodynamics using computational fluid dynamics*, PhD Thesis, October 2002.
- Menzies R.D.D. (2002b) *Validation of the Simulation of Flow in an S-Duct*, 20<sup>th</sup> AIAA Applied Aerodynamics Conference, 24-26 June, St. Louis Missouri.
- Fluid Dynamics Panel Working Group 13. (1991) *Test case 3- subsonic/transonic circular intake*, Advisory Report 270, AGARD September 2002.
- Küçük U.C. (2015) *Passive Flow Control in Boundary Layer Ingesting Semi Submerged Inlet*, MSc Thesis, May 2015.
- Reichert, B. A., and Wendt, B. J., "Improving Curved Subsonic Diffuser Performance with Vortex Generators," AIAA Journal, Vol. 34, No. 1, 1996, pp. 65–72
- Tanguy, G., MacManus D. G., Zachos P. & Gil-Prieto D., "Passive Flow Control Study in an S-Duct Using Stereo Particle Image Velocimetry," AIAA Journal, Vol. 55, No. 6, June 2017
- Chung, J. & Cole, G. L. (1995) *Comparison of Compressor Face Boundary Conditions for Unsteady CFD Simulations*, AIAA Paper, 95-3590
- Wellborn, S. R., Reichert, B. A., and Okiishi, T. H., "Study of the Compressible Flow in a Diffusing S-Duct," Journal of Propulsion and Power, Vol. 10, No. 5, 1994, pp. 668–675.